

1 *Fermi* **LAT** and *WMAP* observations of the supernova remnant
2 **HB 21**

3 G. Pivato^{1,2,3}, J. Hewitt^{4,5,6}, L. Tibaldo^{7,8}, F. Acero⁵, J. Ballet⁹, T. J. Brandt⁵,
4 F. de Palma^{10,11}, F. Giordano^{10,11}, G.H Janssen¹², G. Jóhannesson¹³, D. A. Smith¹⁴

5 Received _____; accepted _____

¹Dipartimento di Fisica e Astronomia “G. Galilei”, Università di Padova, I-35131 Padova,
Italy

²Istituto Nazionale di Fisica Nucleare, Sezione di Padova, I-35131 Padova, Italy

³email: giovanna.pivato@pd.infn.it

⁴CRESST, University of Maryland, Baltimore County, Baltimore, MD 21250

⁵NASA Goddard Space Flight Center, Greenbelt, MD 20771, USA

⁶email: john.w.hewitt@nasa.gov

⁷W. W. Hansen Experimental Physics Laboratory, Kavli Institute for Particle Astro-
physics and Cosmology, Department of Physics and SLAC National Accelerator Laboratory,
Stanford University, Stanford, CA 94305, USA

⁸email: ltibaldo@slac.stanford.edu

⁹Laboratoire AIM, CEA-IRFU/CNRS/Université Paris Diderot, Service d’Astrophysique,
CEA Saclay, 91191 Gif sur Yvette, France

¹⁰Dipartimento di Fisica “M. Merlin” dell’Università e del Politecnico di Bari, I-70126
Bari, Italy

¹¹Istituto Nazionale di Fisica Nucleare, Sezione di Bari, 70126 Bari, Italy

¹²University of Manchester, Manchester, M13 9PL, UK

¹³Science Institute, University of Iceland, IS-107 Reykjavik, Iceland

¹⁴Centre d’Études Nucléaires de Bordeaux Gradignan, IN2P3/CNRS, Université Bordeaux
1, BP120, F-33175 Gradignan Cedex, France

Abstract

We present the analysis of *Fermi* Large Area Telescope (LAT) γ -ray observations of HB 21 (G89.0+4.7). We detect significant γ -ray emission associated with the remnant: the flux > 100 MeV is 9.4 ± 0.8 (stat) ± 1.6 (syst) $\times 10^{-11}$ erg cm $^{-2}$ s $^{-1}$. HB 21 is well modeled by a uniform disk centered at $l = 88^{\circ}75 \pm 0^{\circ}04$, $b = +4^{\circ}65 \pm 0^{\circ}06$ with a radius of $1^{\circ}19 \pm 0^{\circ}06$. The γ -ray spectrum shows clear evidence of curvature, suggesting a cutoff or break in the underlying particle population at an energy of a few GeV. We complement γ -ray observations with the analysis of the *WMAP* 7-year data from 23 to 93 GHz, achieving the first detection of HB 21 at these frequencies. In combination with archival radio data, the radio spectrum shows a spectral break which helps to constrain the relativistic electron spectrum, hence parameters of simple non-thermal radiation models. In one-zone models multiwavelength data favor the origin of γ rays from nucleon-nucleon collisions. A single population of electrons cannot produce both γ rays through bremsstrahlung and radio emission through synchrotron radiation. A predominantly inverse-Compton origin of the γ -ray emission is disfavored because it requires lower interstellar densities than are inferred for HB 21. In the hadronic-dominated scenarios accelerated nuclei contribute a total energy of $\sim 3 \times 10^{49}$ ergs, while in a two-zone bremsstrahlung-dominated scenario the total energy in accelerated particles is $\sim 1 \times 10^{49}$ ergs.

Subject headings: cosmic rays – acceleration of particles – ISM: individual (HB 21) – radiation mechanisms: non-thermal

1. Introduction

Diffusive shock acceleration in supernova remnants (SNRs) is strongly advocated as the mechanism responsible for the acceleration of Galactic cosmic rays (CRs, e.g. Drury 2012). High-energy emission from SNRs is a powerful probe of this process (Reynolds 2008). In particular, high-energy γ -ray emission can pinpoint the presence of energetic leptons or ions, constraining the acceleration efficiency and the maximum energy of accelerated particles (e.g. Aharonian et al. 2007; Abdo et al. 2011; Acciari et al. 2011; Giordano et al. 2012).

SNRs interacting with dense molecular clouds are expected to be bright γ -ray sources (e.g., Hewitt et al. 2009). Archetypal remnants of this class are IC 443 and W44, for which GeV- and, for the former, TeV-energy γ -ray emission are observed and interpreted as the signature of collisions between accelerated nuclei and interstellar matter (Abdo et al. 2010d; Albert et al. 2007; Abdo et al. 2010c), as recently confirmed by the detection of the characteristic spectral feature of γ -rays produced from the decay of neutral pions (Giuliani et al. 2011; Ackermann et al. 2013a).

Both sources belong to a class of objects known as mixed-morphology (MM) SNRs, where an outer shell revealed by non-thermal radio emission surrounds a central region filled by thermal gas emitting in X-rays (Rho & Petre 1998). There is a strong association between MM SNRs and evidence for interactions between shock fronts and dense clouds revealed by OH masers (Yusef-Zadeh et al. 2003). Therefore, MM SNRs are good candidates to be bright γ -ray sources. Indeed, in addition to W44 and IC 443, other members of this class are known to be GeV γ -ray emitters: W28 (Abdo et al. 2010a), W49B (Abdo et al. 2010b), W51C (Abdo et al. 2009a) and 3C 391 (Castro & Slane 2010).

HB 21 (also known as G89.0+4.7, Green 2009) is a MM SNR interacting with molecular clouds. Evidence for interaction comes from several different wavelengths. X-ray observations with *Einstein* provide evidence that the SN explosion took place

35 in a low-density cavity, therefore suggesting a massive stellar progenitor (Knoedlseder
36 et al. 1996). HB 21 has a radio shape with bright filaments and indentations suggesting
37 interactions with the nearby clouds (Byun et al. 2006). Looking at the CO distribution it
38 is possible to distinguish two different structures based on the velocity of the molecular
39 clouds. Koo & Heiles (1991) report the presence of broad CO lines emitted from shocked
40 clumps of molecular gas with high column densities. Infrared line observations (Shinn et al.
41 2009) reveal an infrared spectrum from H₂ gas with a mixture of temperatures, indicating
42 shocks into a multi-phase medium, typical of molecular clouds.

43 The distance to HB 21 was first estimated to be 0.8 kpc on the basis of an association
44 with the Cygnus OB7 complex and ROSAT observations of X-ray absorption (Leahy &
45 Aschenbach 1996). Considering the preshock velocities, the X-ray absorbing column density,
46 the H I and CO distribution along the line of sight and the highly polarized emission, the
47 distance was later determined to be ~ 1.7 kpc (Byun et al. 2006). In this work we adopt the
48 later, revised distance.

49 The age of the SNR is also uncertain. Lazendic & Slane (2006) determine an age of
50 ~ 5600 years by fitting evolutionary models to the thermal X-ray spectrum of the SNR.
51 However, this results from assuming that the SNR is located at 0.8 kpc, and still in the
52 adiabatic phase. Kinematics of the H I shell velocity of 124 km s^{-1} indicates a much older
53 age for the remnant of 4.5×10^4 yr (Koo & Heiles 1991). Additionally, H₂ spectra indicate
54 steady-state continuous shocks, which require $\sim 10^4$ yr to develop (Flower & Pineau des
55 Forêts 1999). In at least some regions optical filaments are observed with line ratios typical
56 of velocities $\sim 150 \text{ km s}^{-1}$, indicating that the shock has evolved into the radiative phase
57 (Mavromatakis et al. 2007). A SNR shock propagating into a uniform medium of $\sim 1 \text{ cm}^{-3}$
58 becomes radiative at an age of $\sim 3.6 \times 10^4$ yr (Mavromatakis et al. 2007). Given this
59 evidence, we argue that HB 21 is a middle-aged SNR, at an age of a few tens of thousands

60 of years, similar to other SNRs interacting with molecular clouds detected by *Fermi* Large
61 Area Telescope (LAT).

62 High-energy γ -ray sources coincident with HB 21 were reported in the 2-year Catalog of
63 the LAT on board the *Fermi Gamma-ray Space Telescope* (Nolan et al. 2012). Three sources
64 are associated with the remnant (2FGL J2043.3+5105, J2046.0+4954, and J2041.5+5003)
65 and an additional source is present on the edge (2FGL J2051.8+5054): we will investigate
66 if it is part of the emission of the remnant or it is a source itself. Reichardt et al. (2012)
67 recently reported an analysis of 3.5 years of *Fermi* LAT data towards HB 21, finding
68 evidence for extended emission and claiming a softer spectrum in the direction of a shocked
69 cloud in the north-western region of the remnant.

70 Due to the large apparent size ($\sim 2^\circ$) this object is well suited for a detailed
71 morphological study using *Fermi* LAT data. Therefore, it is ideal to further assess the
72 correlation between cloud-interacting shocks and γ -ray emission as a tracer of particle
73 acceleration in MM SNRs, as well as to investigate the possible spectral variations that
74 could shed light on the poorly known processes of particle escape from the shocks (e.g.
75 Gabici et al. 2009).

76 In this paper we present the analysis of ~ 4 years of LAT observations of HB 21 and
77 we discuss the γ -ray emission mechanism in light of a new analysis of *WMAP* 7-years
78 data, as well as of archival radio data. In §2 we describe the γ -ray observations and the
79 morphological and spectral characterization of the γ -ray emission from HB 21. In §3 we
80 present the analysis of the *WMAP* and archival radio data, which reveals a break in the
81 high-frequency radio spectrum. In §4 the interpretation of these results is discussed.

2. Gamma-ray analysis

2.1. Observations

The *Fermi* LAT is a pair-conversion γ -ray telescope detecting photons from 20 MeV to > 300 GeV (Atwood et al. 2009). Its on-orbit calibration is described in Abdo et al. (2009b) and Ackermann et al. (2012b) along with the event classification and instrument performance.

For this analysis, data are accumulated from the beginning of scientific operations on 2008 August 4 to 2012 June 14, selecting the low-background P7SOURCE event class. The data analysis was performed using the LAT *Science Tools* package (v9r27p1), available from the *Fermi* Science Support Center¹. For the morphological characterization we use only events with energy >1 GeV to profit from the narrower point-spread function (PSF) in order to separate the γ -ray emission associated with HB 21 from neighboring sources and interstellar emission. We then use events down to 100 MeV to determine the spectral energy distribution of the remnant. Below this energy the PSF becomes much broader than the SNR and the uncertainties related to the instrument response are larger. In both the morphological and spectral characterization we consider photons with measured energies up to 300 GeV, but only find a significant detection of the source up to energies of several GeV due to the limited number of events at high energies.

We perform the analysis in a $10^\circ \times 10^\circ$ region of interest (RoI) centered at the radio position of HB 21 ($l = 89^\circ 0$, $b = +4^\circ 7$). The RoI approximately corresponds to the 68% event containment region for the P7SOURCE events at 100 MeV and exceeds the 95% event containment region for energies $\gtrsim 700$ MeV. We adopted this narrower than usual RoI in order to limit at the lowest energies the large uncertainties due to the modeling of the

¹<http://fermi.gsfc.nasa.gov/ssc>

105 bright interstellar emission from the nearby Cygnus region (Ackermann et al. 2011, 2012c).
106 We also exclude a few time intervals when the LAT boresight was rocked with respect to
107 the local zenith by more than 52° (mostly for calibration purposes or to point at specific
108 sources) and events with a reconstructed angle with respect to the local zenith $>100^\circ$ in
109 order to limit the contribution from the Earth’s atmospheric γ -ray emission. To take into
110 account the latter selection criterion in the calculation of the exposure, we exclude time
111 intervals when any part of the RoI was observed at zenith angles $>100^\circ$.

112 **2.2. Background model and analysis method**

113 The background is composed of diffuse emission and individual nearby γ -ray sources.
114 Diffuse emission is taken into account using the standard models provided by the *Fermi*
115 LAT collaboration² for the P7SOURCE selection (see Nolan et al. 2012). They include
116 a model that accounts for the Galactic interstellar emission from CR interactions with
117 interstellar gas and low-energy radiation fields, and an isotropic background spectrum
118 that accounts for diffuse γ -ray emission of extragalactic origin and residual background
119 events due to charged particle interactions in the LAT misclassified as γ -rays. We leave the
120 normalization of the Galactic interstellar model as a free parameter, yet fix the isotropic
121 background spectrum because it is difficult to separate it from the other components in
122 such a small RoI and it is more reliably determined over larger regions of the sky.

123 We include in the background model all the point sources present in the 2FGL catalog
124 (Nolan et al. 2012) with distances less than 15° from the RoI center and which are not
125 associated with the SNR. We will discuss in §2.4 the case of the source 2FGL J2051.8+5054,
126 which is located at the edge of the SNR. The spectral models used for background sources

² <http://fermi.gsfc.nasa.gov/ssc/data/access/lat/BackgroundModels.html>

127 are those reported in the 2FGL catalog. Fluxes and spectral indices are left as free
 128 parameters in the fit if the source is within the RoI. Otherwise they are fixed to the catalog
 129 values.

130 The background model and the various models for HB 21 are fitted to the LAT data
 131 using a binned maximum-likelihood method based on Poisson statistics (e.g. Mattox et al.
 132 1996), as implemented in the *glike* tool. For this purpose data were binned on an angular
 133 grid with 0°:1 spacing, and different binning in energy as detailed below. The analysis uses
 134 the post-launch instrument response functions (IRFs) P7SOURCE_V6 (Ackermann et al.
 135 2012b).

136 Finally, we note that the radio pulsar J2047+5029 is 0°:5 away from the remnant’s
 137 radio center (Janssen et al. 2009). While pulsars represent the largest Galactic γ -ray source
 138 class, this particular pulsar likely contributes no detectable flux to the ROI. The spindown
 139 power is $\dot{E} \sim 2 \times 10^{33} \text{ erg s}^{-1}$, lower than that of any known γ -ray pulsar, and three times
 140 lower than for any young, radio-loud γ -ray pulsar (Abdo et al. 2013). That is, the pulsar is
 141 probably below the “deathline” expected from the outer magnetospheric emission models
 142 that best describe the LAT pulsars (Wang & Hirotani 2011). Furthermore, the pulsar’s
 143 dispersion measure indicates a distance $D = 4.4 \text{ kpc}$. The ratio $\sqrt{\dot{E}}/D^2 = 2.3 \times 10^{15} \text{ erg}^{1/2}$
 144 kpc^{-2} (a proxy of the expected γ -ray luminosity) is five times lower than for any known
 145 γ -ray pulsar (see Fig. 15 in Abdo et al. 2013). The two-year LAT catalog shows no point
 146 source at the pulsar position (Nolan et al. 2012), nor does the 4-year catalog currently
 147 in preparation. Nevertheless, we searched PSR J2047+5029 for γ -ray pulsations. It is
 148 not part of *Fermi*’s pulsar timing campaign (Smith et al. 2008), so we obtained a timing
 149 solution based on Westerbork Synthesis Radio Telescope (SRT) and Jodrell Bank radio
 150 data taken concurrently with the *Fermi* data³. The ephemeris will be presented in future

³Janssen, and Stappers private communication

151 work (Janssen et al. 2013). We used it to phase-fold the LAT data, over a grid of minimum
 152 energy cuts (100 MeV to 1000 MeV, in 50 MeV steps) and maximum radius cuts (from
 153 0.4 to 2° from the pulsar position, in 0.1 steps). For pulsars with unknown γ -ray spectral
 154 shapes and unknown pulse profile shapes, such grids amount to a search for the maximum
 155 pulsar signal-to-background noise ratio. At each grid location, we calculated the H-test,
 156 which never exceeded 3σ statistical significance (see Section 5 in Abdo et al. 2013). The
 157 pulsar’s energy flux above 100 MeV is therefore lower than for any known γ -ray pulsar,
 158 that is, below 2×10^{-12} erg cm $^{-2}$ s $^{-1}$. We conclude that the pulsar can be neglected when
 159 characterizing γ -ray emission from HB 21.

160 **2.3. Systematic uncertainties**

161 Two major sources of systematic errors on the results are the uncertainties in the LAT
 162 effective area and the modeling of interstellar emission. The uncertainties in the effective
 163 area for the IRFs we use are evaluated as 10% at 100 MeV, 5% at 516 MeV, and 10% above
 164 10 GeV, linearly varying with the logarithm of energy between those values (Ackermann
 165 et al. 2012b). We estimate the error induced in the characterization of the γ -ray fluxes of
 166 HB 21 by repeating the analysis with two sets of modified IRFs where the effective area
 167 was upscaled or downscaled by its uncertainty. This approach neglects errors induced by
 168 possibly more complicated variations of the effective area and, therefore, does not capture
 169 uncertainties in the spectral shape of the source. However, this is sufficient for our purpose
 170 since, as discussed in section 2.5, for HB 21 systematic uncertainties are dominated by the
 171 modeling of interstellar emission.

172 To gauge the systematic uncertainties due to the interstellar emission model we
 173 compare the results obtained using the standard model in §2.2 with the results based on
 174 eight alternative interstellar emission models. The alternative emission models are based

175 on a subsample of those examined by Ackermann et al. (2012a). We varied some of the
 176 most important parameters of the interstellar emission models, namely the uniform spin
 177 temperature used to estimate the column densities of interstellar atomic hydrogen (150 K
 178 and 10^5 K, the latter being equivalent to the small optical depth approximation), the
 179 vertical height of the CR propagation halo (4 kpc and 10 kpc), the CR source distribution
 180 in the Galaxy (the pulsar distribution by Lorimer et al. 2006 and the SNR distribution by
 181 Case & Bhattacharya 1998⁴). In this way we built a grid of eight alternative interstellar
 182 emission models. We refer the reader to Ackermann et al. (2012a) for further details
 183 about the modeling strategy and multimessenger/multiwavelength constraints on these
 184 parameters.

185 Each of these models was fitted to the whole-sky P7SOURCE data in the energy
 186 range between 100 MeV and 300 GeV using the maximum likelihood method described
 187 in Ackermann et al. (2012a). We determine independent log-parabolic re-normalization
 188 functions separately for the Inverse Compton (IC) component and the components
 189 associated to atomic hydrogen and molecular hydrogen (traced by CO), split along the line
 190 of sight into four broad Galactocentric annuli between 0–4 kpc, 4–8 kpc, 8–10 kpc (the local
 191 annulus) and 10–30 kpc.

192 The eight resulting models were used to repeat the source analysis described in §2.4,
 193 for the determination of the disk dimension, and §2.5 for the spectral analysis of the source.
 194 In each of the iterations we replaced the standard isotropic background and Galactic
 195 interstellar emission models with the alternative isotropic background spectra and Galactic
 196 interstellar emission templates, independently for the sub-components described above

⁴The validity of the Case & Bhattacharya (1998) $\sigma - D$ relation has been criticised: it is used in Ackermann et al. (2012a) as an alternative to probe the effect of changing the CR distribution.

197 (note that for the line of sight of HB 21 only the two outermost Galactocentric annuli are
 198 relevant). For the same reasons as for the standard model, we fix the isotropic background
 199 spectrum. We leave free the normalization parameters of the interstellar model components
 200 in the third and fourth ring, and of the IC component. Through this procedure we explored
 201 the impact of adopting a different model-construction strategy, of varying the model
 202 parameters and of allowing more freedom in the fit. We stress that we explored only some
 203 of the uncertainties related to the modeling of interstellar emission, but we are nevertheless
 204 able to obtain an indication about some important systematic effects. A more thorough
 205 discussion on this method for exploring the systematic uncertainties due to the modeling of
 206 diffuse emission is available in de Palma et al. (2013).

207 2.4. Morphological analysis

208 In Figure 1a we show a count map of the RoI for energies >1 GeV, to visually illustrate
 209 the morphology of the γ -ray emission in the region. We consider different spatial models
 210 for the emission from HB 21, summarized in Table 1. For each model we evaluate the test
 211 statistic

$$TS = 2(\ln \mathcal{L}_1 - \ln \mathcal{L}_0) \quad (1)$$

212 where \mathcal{L}_1 is the maximum-likelihood value for the model including the remnant and \mathcal{L}_0
 213 is the maximum-likelihood value for the model not including it (null hypothesis). If the
 214 null hypothesis is verified (no γ -ray emission associated to HB 21), TS is expected to be
 215 distributed as a χ^2 with a number of degrees of freedom given by the additional number of
 216 free parameters in the model including the source, with the caveats discussed in Protasov
 217 et al. (2002).

218 We determine the position and extension of the γ -ray emission associated with HB 21
 219 from γ -ray data only using the *pointlike* tool, which is optimized and widely validated

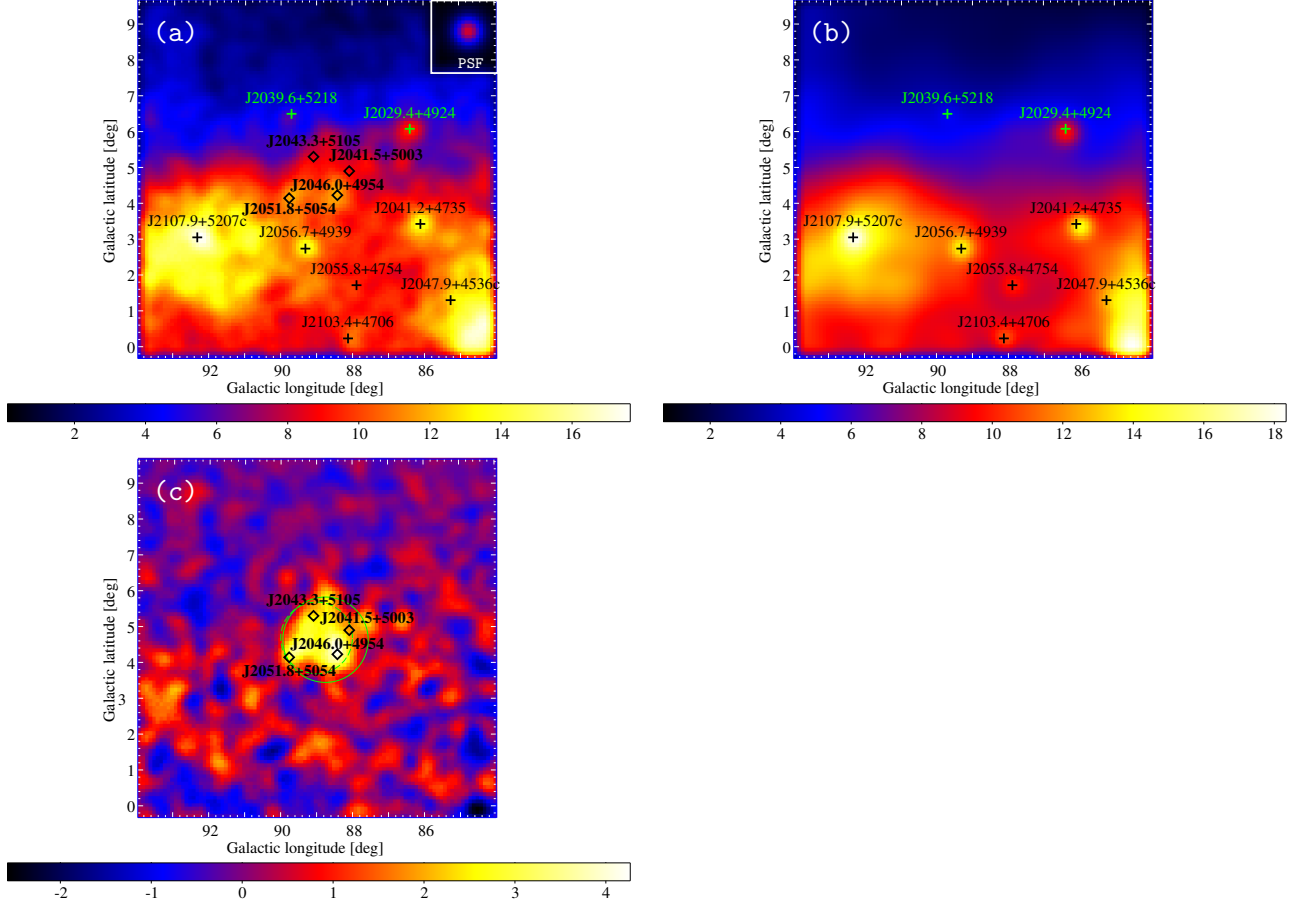


Fig. 1.— a) LAT counts map at energies > 1 GeV with color scale in counts/pixel. We overlaid the positions of 2FGL sources (crosses for background sources and bold diamonds for the three sources associated with the remnant and 2FGL J2051.8+5054). The inset in the top right corner shows the effective PSF over the energy range considered for a power-law spectral distribution with index 3.1. b) Background model map (calculated using the best-fit parameters from the case where HB 21 was modeled as a disk). c) Remaining emission associated with HB 21; overlaid are the positions of the four point sources above, the best-fit disk (solid line) and the radio disk (dashed line). The pixel size is $0^\circ.1$ and all maps are smoothed for display with a Gaussian kernel of $\sigma=0^\circ.4$.

220 against Monte Carlo simulations for this purpose (Lande et al. 2012). We model the source
 221 as a disk with a power-law spectrum and we determine the position of its center (l, b) and
 222 radius r , along with flux and spectral index from LAT data, using an energy binning of
 223 eight bins per decade. We considered both the cases where 2FGL J2051.8+5054 is included
 224 as a separate point source in the model or removed. In the first case we obtain the best fit
 225 parameters: $l = 88^{\circ}62 \pm 0^{\circ}05$, $b = 4^{\circ}79 \pm 0^{\circ}06$, and $r = 1^{\circ}14 \pm 0^{\circ}07$. In the second we have
 226 $l = 88^{\circ}75 \pm 0^{\circ}04$, $b = 4^{\circ}65 \pm 0^{\circ}06$, $r = 1^{\circ}19 \pm 0^{\circ}06$. Errors reflect statistical uncertainties
 227 only. The TS for the case including separately 2FGL J2051.8+5054 in the model is larger
 228 by 14 than the case with the disk only (Table 1). The significance of the separate source
 229 hypothesis is below the threshold usually required to claim a detection for LAT sources
 230 ($TS > 25$). Deeper observations are needed to determine if 2FGL J2051.8+5054 can be
 231 distinguished as a source independent from the remnant. In the rest of the paper, we do
 232 not consider 2FGL J2051.8+5054 as a separate source and, therefore, we remove it from the
 233 model. We note that the results concerning the morphology of HB 21 are robust regardless
 234 of whether 2FGL J2051.8+5054 is included as a separate source in the model or not. Using
 235 the best fit disk, the significance of the detection of HB 21 is $\sim 29 \sigma$. We also check whether
 236 the source size changes with energy by separately fitting a disk to the LAT data from 1 to
 237 3 GeV and from 3 to 10 GeV. We obtain $r = 1^{\circ}19 \pm 0^{\circ}09$ in the lower-energy range and
 238 $r = 1^{\circ}24 \pm 0^{\circ}09$ in the higher-energy range. No significant change in size with energy is
 239 detected.

240 In Figure 1b we show the background model map obtained from the fit with the disk,
 241 and in Figure 1c the background-subtracted count map where the emission associated to
 242 HB 21 is visible. If we compare the TS with the model in which HB 21 is modeled by the
 243 four point sources in the 2FGL Catalog (Table 1) we find that the extended source provides
 244 a higher likelihood for a lower number of free parameters in the fit. Therefore, we conclude
 245 that the hypothesis of extended emission is preferred over four individual point sources.

246 We then calculate the systematic uncertainties related to interstellar emission using the
 247 alternative models as described in §2.3. When the alternative interstellar emission models
 248 are used, the γ -ray disk is systematically shifted toward the north-west part with respect to
 249 the radio shell (with shifts in longitude between $0^\circ.19$ and $0^\circ.24$, and in latitude between $0^\circ.06$
 250 and $0^\circ.09$), and the disk radius is systematically smaller by $0^\circ.18$ – $0^\circ.24$, but the significance
 251 of the detection of HB 21 does not change sizably. This effect is mainly due to the different
 252 approaches used to deal with the dark gas, neutral interstellar gas which is not well traced
 253 by the linear combination of column densities inferred from the 21-cm H I line and the
 254 2.6-mm CO line, but which is traced by correlated residuals in dust emission/absorption
 255 and interstellar γ -ray emission (Grenier et al. 2005). Dust residuals are used as a dark-gas
 256 template fitted to the γ -ray data in the standard interstellar model, whereas they are used
 257 to correct the H I column densities in the alternative models assuming a dust-to-gas ratio
 258 independent from γ -ray observations. This leads to different estimates of the gas column
 259 densities, therefore to different structures in the interstellar emission models. Additionally,
 260 the standard model accounts for enhanced interstellar emission toward the nearby Cygnus X
 261 complex (see Ackermann et al. 2011, 2012c), whereas the alternative models do not.
 262 These differences are found to have a significant impact on the determination of the SNR
 263 morphology. We note that for all the alternative models the disk extends beyond the rim of
 264 the remnant in coincidence with the western molecular cloud, but leave the faint south-east
 265 edge of the radio shell off.

266 In Figure 2 we compare the γ -ray emission associated with HB 21 to emission from the
 267 remnant at other wavelengths. Figure 2a compares the γ -ray image with radio emission at
 268 6-cm tracing non-thermal electrons (see later §3). Figure 2b compares the γ -ray morphology
 269 with X-ray emission from the thermal plasma filling the center of the remnant, measured by
 270 ROSAT (Voges et al. 1999). The ROSAT image was cleaned using the standard background

Table 1. Test statistic (TS) and degrees of freedom (d.o.f.) for the different spatial models for the γ -ray emission associated to HB 21 considered in 2.4.

sources	TS	d.o.f.
Null hypothesis	0	0
4 point sources	256	10
disk	302	5
disk + 2FGL J2051.8+5054	316	7
X-ray image	212	2
X-ray image+ 2FGL J2051.8+5054	234	4
radio image	298	2
radio image + 2FGL J2051.8+5053	312	4

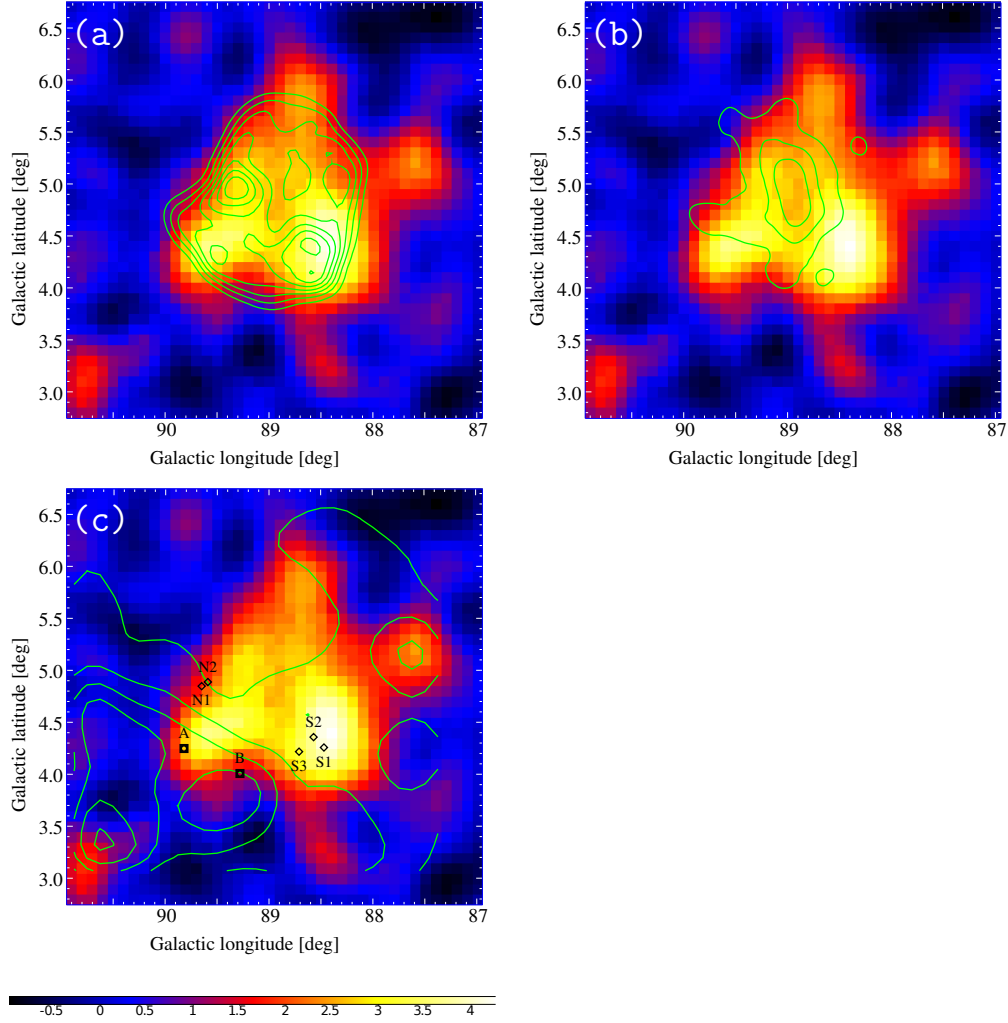


Fig. 2.— Emission associated with HB 21 (Fig. 1c) overlaid with contours from emission at other wavelengths (see text for details): a) Radio emission intensity at 6-cm with a beam size of $0^{\circ}.16$, smoothed with a Gaussian kernel with $\sigma=0^{\circ}.2$. The seven contour levels are linearly spaced from 0 to 2.0 Jy beam^{-1} . b) Background-subtracted X-ray emission (ROSAT) smoothed with a Gaussian kernel of $\sigma = 0^{\circ}.25$. The three contour levels are linearly spaced from 0.36×10^{-3} to $2.13 \times 10^{-3} \text{ counts s}^{-1} \text{ arcmin}^{-2}$. c) Intensities of the 2.6-mm CO line in the Local-Arm region. The six contour levels are linearly spaced from 1.5 K km s^{-1} to 28 K km s^{-1} . We also show the positions of the shocked CO clumps (diamonds) and clouds A and B (squares) given in Koo & Heiles (1991).

271 maps⁵. Finally Figure 2c compares the γ -ray emitting region with the distribution of
 272 molecular material. Molecular column densities in the Local-Arm region are traced by the
 273 CO line intensities at 2.6-mm (Dame et al. 2001; Dame & Thaddeus 2011) integrated over
 274 velocities with respect to the local standard of rest within ± 20 km s⁻¹. We also show the
 275 positions of shocked CO clumps and of two large CO clouds distributed along the boundary
 276 of the radio shell (Koo & Heiles 1991). The γ -ray emission associated with HB 21 is broader
 277 than the central region filled by thermal X-ray emitting plasma. It compares well with the
 278 radio shell, but appears to extend beyond the radio shell in regions where molecular clouds
 279 are present. The brightest γ -ray regions coincide with the Southern shocked CO clumps
 280 identified by Koo & Heiles (1991). This correlation with CO suggests that at least part of
 281 the γ -ray emission from HB 21 may be produced by accelerated particles colliding with
 282 dense interstellar matter.

283 To quantitatively assess the correlation between γ -ray, X-ray and radio emission from
 284 HB 21 we use the X-ray and radio images as templates in the γ -ray analysis. For both
 285 templates we compare the cases when 2FGL J2051.8+5054 is included in the fit as a
 286 background source or not. All the spatial templates are fitted with a power-law spectrum.
 287 From the results reported in Table 1 we confirm that the morphology of the remnant
 288 in γ -rays significantly differs, as expected, from the emission in X-rays. Both the radio
 289 template and the γ -ray disk provide a good fit to the data, though the first has less degrees
 290 of freedom, as shown in Table 1. Since the two models are not nested it is not possible to
 291 conclude which is the best one. Given that the disk model provides the largest TS of all
 292 single source models, and is derived from the γ -ray data, we use this model to compute the
 293 spectrum of the remnant.

⁵Available from <http://www.xray.mpe.mpg.de/cgi-bin/rosat/rosat-survey>

2.5. Spectral analysis

The spectral energy distribution (SED) of HB 21 is determined over the full energy range between 100 MeV and 300 GeV (using 35 logarithmic energy bins for the likelihood analysis) by modeling the remnant with the best-fit disk. We compare the hypotheses of a power law

$$\frac{dN}{dE} = N_0 \left(\frac{E}{100 \text{ MeV}} \right)^{-\Gamma} \quad (2)$$

with three different curved spectral models in order to quantify deviations from the former. The three functional forms are:

1. log-parabola.

$$\frac{dN}{dE} = N_0 \left(\frac{E}{1000 \text{ MeV}} \right)^{-(\alpha + \beta \ln(E/1000 \text{ MeV}))} \quad (3)$$

2. smooth broken power law

$$\frac{dN}{dE} = N_0 \left(\frac{E}{100} \right)^{-\Gamma_1} \left(1 + \left(\frac{E}{E_b} \right)^{(\Gamma_2 - \Gamma_1)/0.2} \right)^{-0.2} \quad (4)$$

with Γ_1 and Γ_2 being the spectral indices below and above the break energy E_b , respectively

3. power law with exponential cutoff

$$\frac{dN}{dE} = N_0 \left(\frac{E}{200 \text{ MeV}} \right)^{-\Gamma} \exp \left(-\frac{E}{E_c} \right) \quad (5)$$

where E_c is the cutoff energy.

In Table 2 we report the TS values and the additional degrees of freedom for the curved spectral models compared to the power law. All the curved models have a higher TS than the power law distribution. For the following discussion we adopt the log-parabola because it yields the largest improvement with respect to the simple

Table 2. TS and additional degrees of freedom for the different functions used to model the SED of HB 21. For each model we report the values of the best-fit parameters.

spectrum shape	ΔTS	additional d.o.f.	Fit parameters
power law	0	0	$\gamma=2.33\pm 0.03$
log-parabola	92	1	$\alpha = 2.54 \pm 0.05$ $\beta = 0.39 \pm 0.04$
smooth broken power law	41	2	$\gamma_1=1.67\pm 0.02$ $\gamma_2=3.54\pm 0.05$ $E_b=789\pm 65$ MeV
power law with exponential cutoff	82	1	$\gamma_1=1.42\pm 0.03$ $E_c=958\pm 41$ MeV

311 power-law, with a $\Delta TS = 92$, corresponding to an improvement at a $\sim 9\sigma$ significance
 312 level in the energy range from 100 MeV to 300 GeV. The total γ -ray energy flux from
 313 HB 21 results to be 9.4 ± 0.8 (stat) ± 1.6 (syst) $\times 10^{-11}$ erg cm $^{-2}$ s $^{-1}$ and the photon
 314 flux 1.48 ± 0.2 (stat) ± 0.4 (syst) $\times 10^{-7}$ ph cm $^{-2}$ s $^{-1}$. The systematic errors shown in
 315 this section are calculated as described in §2.3 and extracting the root mean square of the
 316 variations with respect to the values from the standard model.

317 We also computed the SED in a model-independent way by splitting the energy range
 318 between 0.1 MeV and 60 GeV in 12 logarithmically spaced bins. The model is the same as
 319 described above, but in each narrow energy bin we leave free only the overall fluxes; other
 320 spectral parameters are fixed to the 2FGL values for background sources and to a power-law
 321 index of 2 for HB 21 (the results are insensitive to this particular choice). When TS for an
 322 individual bin is < 9 we calculate an upper limit at the 95% confidence level determined
 323 through the likelihood profile method.

324 We show the resulting SED in Figure 3 with also systematic errors indicated.
 325 Systematic errors due to interstellar emission model are then summed in quadrature with
 326 the error due to the LAT effective area uncertainties (§2.3) for display. The SED points are
 327 reported in Table 3. The contributions due to the modeling of interstellar emission and the
 328 LAT effective area are presented separately. In the energy range considered, the systematic
 329 errors are driven by the interstellar emission model.

330 2.6. Search for spectral variations across the remnant

331 HB 21 is an extended source, located in an area rich in interstellar matter. The
 332 interaction with nearby molecular clouds (Byun et al. 2006) might cause spectral variation
 333 across the SNR, as suggested in the analysis by Reichardt et al. (2012). To further

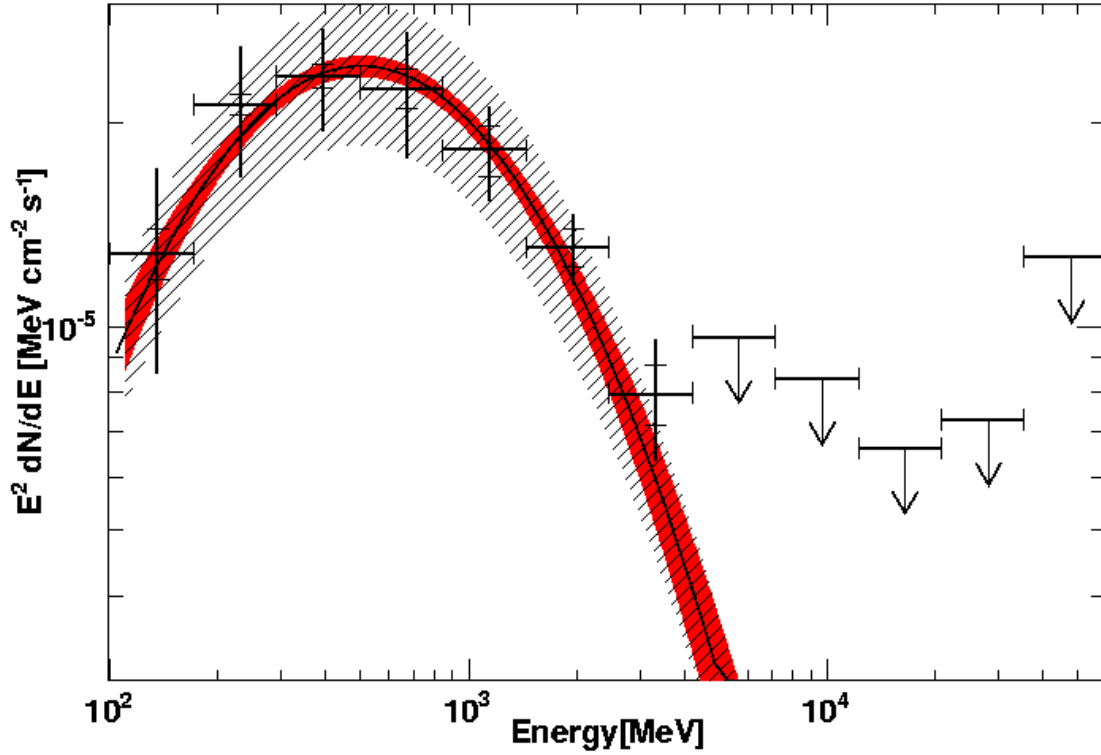


Fig. 3.— Spectral energy distribution of HB 21. The line shows the best-fit log-parabola model, the light-red filled area shows the statistical error band and the dashed gray area shows the systematic uncertainties. The bar markers correspond to statistical errors only, while lines show the larger systematic errors. 95% confidence-level upper limits are given for energy bins where the TS of the source is < 9 .

Table 3. SED of γ -ray emission from HB 21. For each SED point we report the systematic uncertainties separately for those related to interstellar emission modeling (IEM) and LAT effective area (EA), as well as the overall uncertainty obtained by summing them in quadrature.

Energy bin center	$E^2 dN/dE$	Statistical	IEM	EA	Total syst.
[MeV]	[$\text{eV cm}^{-2} \text{s}^{-1}$]	[$\text{eV cm}^{-2} \text{s}^{-1}$]	[$\text{eV cm}^{-2} \text{s}^{-1}$]	[$\text{eV cm}^{-2} \text{s}^{-1}$]	[$\text{eV cm}^{-2} \text{s}^{-1}$]
135	12.8	± 1.1	± 4.1	± 1.2	± 4.3
230	21.3	± 0.8	± 4.3	± 1.8	± 4.7
393	23.5	± 0.9	± 3.8	± 1.6	± 4.1
670	22.5	± 1.5	± 4.6	± 1.1	± 4.8
1143	18.3	± 1.5	± 2.7	± 0.9	± 2.9
1950	13.1	± 0.9	± 1.4	± 0.7	± 1.6
3327	7.9	± 0.8	± 1.5	± 0.5	± 1.6

334 investigate the possibility, we repeat the analysis described in §2.4 after splitting the best-fit
335 disk in several different ways (Figure 4):

- 336 a. radio-emitting area (modeled with a uniform disk centered at $l=89^{\circ}0$ $b=+4^{\circ}7$ with
337 radius 1°) and the remainder of the best-fit disk (Figure 4a);
- 338 b. southern shocked-CO region (modeled as a uniform disk centered at $l=88^{\circ}38$ $b=4^{\circ}50$
339 and radius $0^{\circ}35$) and the remainder of the best-fit disk (Figure 4b);
- 340 c. disk split into two halves to separate the southern shocked CO area from the rest
341 (Figure 4c);
- 342 d. finally, we test the division proposed by Reichardt et al. (2012) splitting the uniform
343 disk into three subregions covering 120° each (Figure 4d).

344 We first perform the analysis above 1 GeV to profit from the narrower PSF. For this
345 configuration we modeled the source spectrum as a simple power law. The results are
346 reported in Table 4. There are no significant improvements in the likelihood from splitting
347 the disk in subregions ($< 2\sigma$). This means that there is no evidence of spectral variations
348 across the γ -ray emitting region. Indeed, the spectral indices of the subregions are all
349 compatible within statistical uncertainties.

350 Then we perform the analysis over the full energy range above 100 MeV. We fit the
351 spectrum of each subregion with a log-parabola function as for the uniform disk. The
352 results are reported in Table 5. Even for this larger energy range we find only marginal
353 evidence ($< 3\sigma$) of spectral variations across the remnant and the values for the spectral
354 parameters are compatible within statistical errors.

355 In conclusion, we do not confirm the claim by Reichardt et al. (2012) of a softer
356 spectrum toward the clouds NW and A. Spectral variations are not significant ($< 3\sigma$),

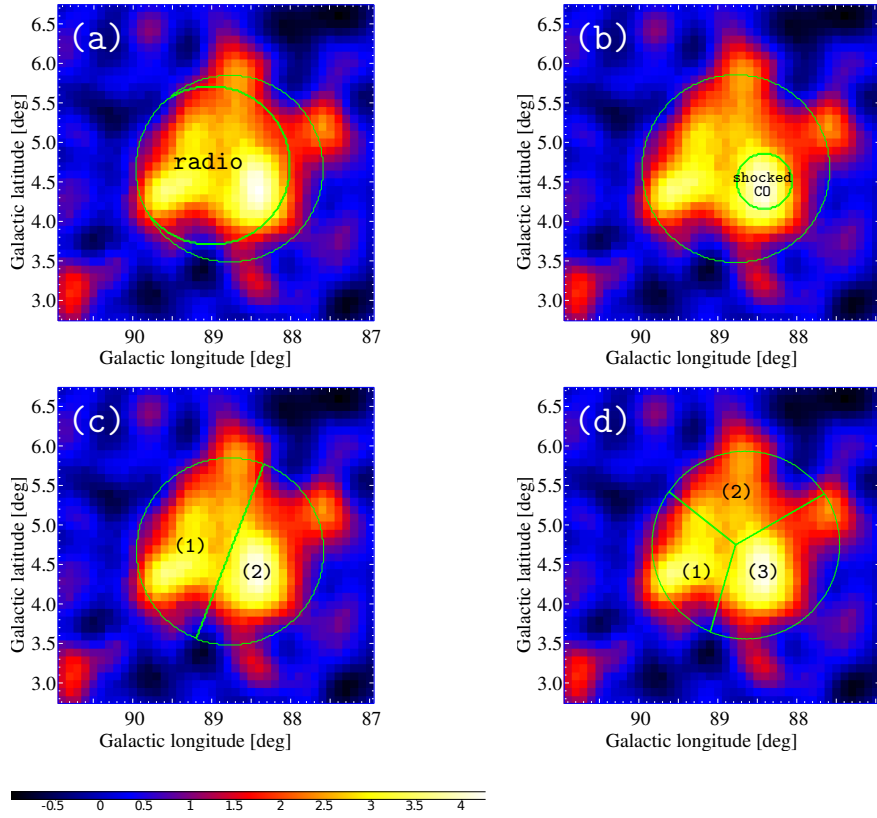


Fig. 4.— Emission associated with HB 21 as in Fig. 1c overlaid with the boundaries of the templates used in the search for spectral variations across the remnant described in 2.6.

Table 4. Likelihood values and spectral indices for the models described in §2.6, splitting the single best-fit disk in different subregions. For each case we report the number of additional degrees of freedom (d.o.f.) and the spectral indices. Analysis performed above 1 GeV.

region splitting	ΔTS	Δ d.o.f.	index 1	index 2	index 3
single disk	0	0	3.09 ± 0.12		
a	2.8	2	2.98 ± 0.12	3.35 ± 0.10	
b	4.2	2	2.88 ± 0.31	3.14 ± 0.15	
c	2.2	2	2.86 ± 0.4	3.29 ± 0.1	
d	1.6	4	2.92 ± 0.22	3.29 ± 0.21	2.95 ± 0.17

Table 5. Likelihood values and spectral indices for the models described in §2.6, splitting the single best-fit disk in different subregions. For each case we report the number of additional degrees of freedom (d.o.f.) and the spectral indices. The analysis is performed above 100 MeV.

region splitting	ΔTS	Δ d.o.f.	α	β
single disk	0	0	2.54 ± 0.05	0.39 ± 0.04
a	13	3	$\alpha_{radio} = 2.41 \pm 0.09$ $\alpha_{other} = 3.48 \pm 0.89$	$\beta_{radio} = 0.37 \pm 0.06$ $\beta_{other} = 0.74 \pm 0.39$
b	13.4	3	$\alpha_{CO} = 2.27 \pm 0.06$ $\alpha_{other} = 2.61 \pm 0.21$	$\beta_{CO} = 0.38 \pm 0.04$ $\beta_{other} = 0.43 \pm 0.03$
c	8	3	$\alpha_1 = 2.47 \pm 0.06$ $\alpha_2 = 2.64 \pm 0.09$	$\beta_1 = 0.36 \pm 0.03$ $\beta_2 = 0.45 \pm 0.03$
d	3	6	$\alpha_1 = 2.35 \pm 0.15$ $\alpha_2 = 2.75 \pm 0.29$ $\alpha_3 = 2.53 \pm 0.18$	$\beta_1 = 0.38 \pm 0.10$ $\beta_2 = 0.39 \pm 0.17$ $\beta_3 = 0.43 \pm 0.13$

357 even considering statistical uncertainties only. More data and a better handling of the
 358 current dominating uncertainties related to the modeling of interstellar emission (that were
 359 neglected in the study of Reichardt et al. 2012) are required in order to further probe for
 360 possible γ -ray spectral variations across HB 21.

361 **3. *WMAP* observations and radio spectrum**

362 The radio morphology of HB 21 is that of a large oblate shell (see contours in Figure
 363 4a). It has both a large angular diameter and high radio flux density, which have made it a
 364 favorable target for telescopes across the radio spectrum. High-resolution imaging reveals
 365 bright filaments and indentations along the periphery (Leahy & Roger 1998). We use the
 366 7-year all-sky data of the *Wilkinson Microwave Anisotropy Probe* (*WMAP*) to extend the
 367 radio spectrum of HB 21 above 10 GHz. Five bands are analyzed with effective central
 368 frequencies (ν_{eff}) of 23 to 93 GHz (Jarosik et al. 2011).

369 The *WMAP* data are fit within a 4° square region with a spatial template plus a
 370 sloping planar baseline (following Hewitt et al. 2012). For the spatial template we use the
 371 map of HB 21 from the Sino-German 6-cm (4.8 GHz) survey (Gao et al. 2011, resolution
 372 of $9.5'$). We include a separate, freely-normalized point source to account for the bright
 373 nearby extragalactic point source 3C 418 (Hill 1974). The templates are smoothed to the
 374 *WMAP* beam at each band (Weiland et al. 2011) and fit to the data.

375 Figure 5 shows an example of the *WMAP* skymap, best-fit model and residual map for
 376 the Q band (61 GHz). Table 6 lists the beam sizes and fitted fluxes with errors estimated
 377 from the RMS of the fit residuals. To ensure that fluxes we extracted from the *WMAP* data
 378 are properly calibrated, we also analyzed the bright radio sources 3C 58 and Cassiopeia A
 379 using the same procedure and find agreement with Weiland et al. (2011). We also note that

380 the addition of a template for 3C 418 does not produce a significant change in the measured
 381 fluxes of HB 21.

382 The global radio spectrum of HB 21 from 38 MHz to 93 GHz is shown in Figure 6. We
 383 include our *WMAP* analysis along with published flux densities from the literature (Kotthes
 384 et al. 2006, and references therein). It is evident that a spectral break is present in the
 385 spectrum at high frequencies. We first fit the radio spectrum with a single power law, $S(\nu)$
 386 $= S_0 \nu^{-\alpha}$ and find a flux normalization at 1 GHz of $S_0 = 201 \pm 3$ Jy and an index $\alpha = 0.50$
 387 ± 0.02 . The fitted index is significantly steeper than $\alpha = 0.38$ determined from fitting only
 388 the data below 10 GHz because it does not account for the break at high frequencies.

389 We therefore include a spectral break of $\Delta\alpha = 0.5$ at a frequency ν_b . This is
 390 appropriate for synchrotron losses in a homogeneous source of continuously injected
 391 electrons, as expected for middle-aged SNRs (Leahy & Roger 1998; Reynolds 2009,
 392 Section 2.1). With one additional free parameter, we can now produce a good fit to the
 393 radio spectrum. We find the spectral break to have a significance of 5.3σ by applying the
 394 F-test to compare the χ^2 fit to that of the simple power-law. The best fit parameters for
 395 the radio spectrum of HB 21 are $\alpha = 0.38 \pm 0.02$ and $\nu_b = 5.9 \pm 1.2$ GHz. Additionally,
 396 we tried to fit the spectrum using a power law with an exponential cutoff of the form, $S(\nu)$
 397 $= S_0 \nu^{-\alpha} \exp(-\nu/\nu_c)$. This produces nearly as good a fit, with $\alpha = 0.34 \pm 0.02$, $\nu_c = 29 \pm$
 398 4 GHz, and a significance of 5.2σ .

399 The radio index, α , is related to the particle index, Γ_p , by $\Gamma_p = 2\alpha + 1$. The observed
 400 radio index below the break $\alpha = 0.38$ gives $\Gamma_p \sim 1.8$, which is similar to the spectral index
 401 obtained with the *Fermi* LAT data in §2.5. We explore physical mechanisms which could
 402 explain both the γ -ray and radio spectra in the discussion in §4.

403 The observed break in the high-frequency spectrum cannot be explained by spectral
 404 variations across HB 21. Leahy (2006) studied spectral variations using radio observations

405 at 408 and 1420 MHz. Manual fits to 36 individual regions across the SNR show variations
 406 between 0.2–0.8, with a mean spectral index of 0.45 and a standard deviation of 0.16. The
 407 brightest regions tend to have an index that is flatter than average and than the canonical
 408 spectral index (0.5) from diffusive shock acceleration. Thus, fitting the radio spectral index
 409 of the flux from the entire remnant leads to an even flatter global index of 0.38.

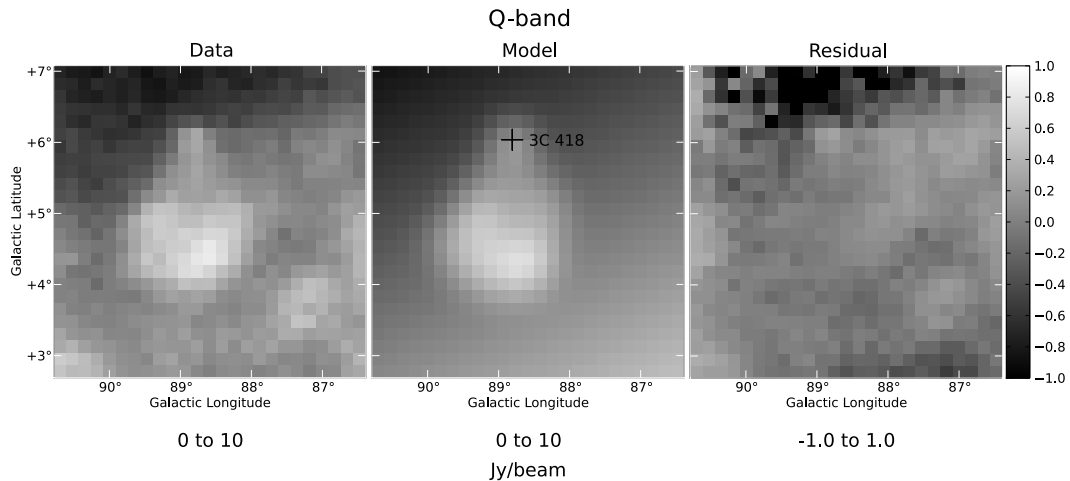


Fig. 5.— Example of the template fit to the *WMAP* data within a 4° square region of HB 21 in the Q band (61 GHz). The three panels present the 7-year skymap image (left), the model resulting from a fit of the radio template plus a sloping planar baseline and a point source at the position of 3C 418 marked by a cross (center), and the fractional residuals (defined as the fit residual divided by the model). The upper and lower limits of the linear color bar are given beneath each image; data and model are on the same scale.

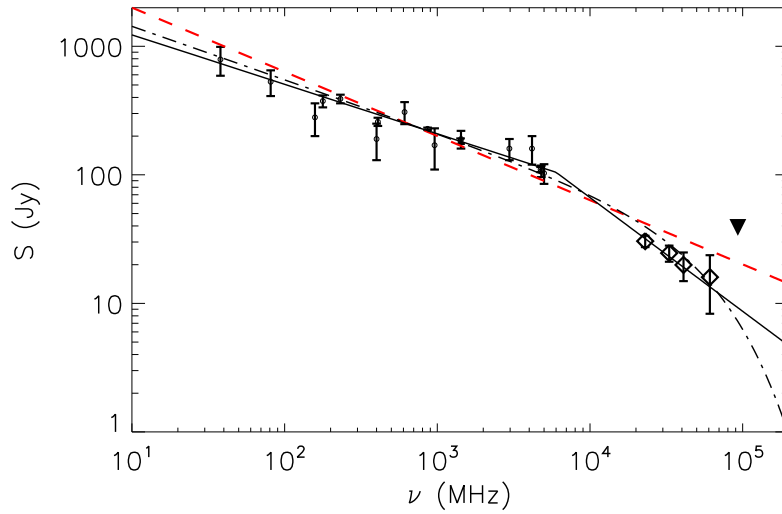


Fig. 6.— Integrated radio flux density of HB 21 as a function of frequency. Data points below 10 GHz, circles, are from the literature (see Kothes, et al. 2006, and references therein). The new *WMAP* data points are shown as open diamonds and presented in Table 6. The upper limit is shown as a downward filled triangle. The dashed red line shows a power-law fit to the entire radio spectrum. The solid black line shows a fit to the data assuming a spectral break as described in the text. The dot-dashed black line shows the fit assuming an exponential cutoff.

4. Discussion

4.1. Non-thermal Modeling

We have identified spatially extended γ -ray emission coincident with SNR HB 21, indicating the presence of relativistic particles. Determining the mechanism responsible for γ -ray emission is crucial in order to measure the underlying particle population accelerated by the SNR. To do so, we model emission from the remnant using *isis*, the *Interactive Spectral Interpretation System* (Houck & Denicola 2000). For arbitrary particle momentum distributions, a suite of interaction models available in the literature is used to calculate the non-thermal emission spectrum (Houck & Allen 2006, and references therein) which is then fit to radio and γ -ray data. We used an updated interaction cross section for hadronic interactions (Karlsson & Kamae 2008). The included prescriptions are in agreement with the results from Sturmer et al. (1997).

To constrain the emitting particle distribution we simultaneously fit radio and γ -ray emission from non-thermal electrons and protons. Initially, we adopt the simplifying assumption that all emission originates from a region characterized by a constant matter density and magnetic field strength. This single emitting zone is assumed to be equal to the size of the remnant derived from the best-fit γ -ray disk. Additionally, the population of accelerated nuclei and electrons is assumed to be described by the same particle distribution, here assumed to follow a power-law with an exponential cutoff of the form $dN/dp \propto \eta_{e,p} p^{-\Gamma_p} \times \exp(-p/p_{\max})$, where η_e/η_p gives the ratio of electrons to protons and p the momentum. The normalization and maximum energy cutoff are left as free parameters, and adjusted to fit the data. An exponential cutoff in the momentum spectra of electrons is expected when energy losses exceed the rate of energy gain from shock acceleration (Webb et al. 1984). In practice, we find that we do not have sufficient spectral coverage to differentiate strongly between an exponential cutoff or a broken power law.

435 To determine the total energy in relativistic particles from the normalization of the
 436 non-thermal emission we must consider the physical conditions of the emitting region.
 437 HB 21 is known to lie in the vicinity of several large molecular clouds. The presence of
 438 optical [S II] but not oxygen line emission indicates slow shocks $<100 \text{ km s}^{-1}$ into ambient
 439 densities of at least 2.5 cm^{-3} (Mavromataki et al. 2007). Shocked CO filaments are
 440 observed with densities of order $\sim 10^2\text{--}10^4 \text{ cm}^{-3}$ and small filling factors ≤ 0.1 (Koo et al.
 441 2001). For neutral gas, the mean ambient HI density for the expanding shell is $\sim 8 \text{ cm}^{-3}$ at
 442 a distance of 1.7 kpc (Koo & Heiles 1991). Reichardt et al. (2012) estimated the molecular
 443 mass within HB 21 by integrating all CO line emission between the velocity range from
 444 $+0$ to -20 km s^{-1} . This estimate likely includes molecular gas outside the SNR, but is a
 445 conservative upper limit. Adopting a distance of 1.7 kpc, the maximum molecular mass
 446 is $5.5 \times 10^4 M_{\odot}$, the diameter of the SNR is 55 pc, and the maximum volume-averaged
 447 molecular gas density is 25 cm^{-3} . Therefore, we assume a gas density of 15 cm^{-3} , noting
 448 that this is uncertain by a factor of a few.

449 There are three primary emission mechanisms to produce γ -ray emission in SNRs. In
 450 the so-called hadronic scenario the emission is dominated by γ -rays radiated through the
 451 decay of π^0 mesons produced in collisions between accelerated nuclei with the ambient
 452 gas. In the leptonic scenarios γ -ray emission results either from IC scattering of relativistic
 453 electrons on low-energy photon fields such as the cosmic microwave background (CMB),
 454 or non-thermal bremsstrahlung. As the matter density is increased, the bremsstrahlung
 455 contribution will rise and dominate over the IC at densities $\gtrsim 1 \text{ cm}^{-3}$, unless the photon field
 456 is greatly amplified above the CMB. HB 21 appears to have a high enough gas density that
 457 bremsstrahlung is expected to dominate over IC emission. In modeling the non-thermal
 458 spectrum of HB 21 we explored models in which the assumed physical conditions are
 459 modified such that each of these three emission mechanisms is dominant.

460 One-zone models for all three scenarios are presented as SED fits in Figure 7.
 461 Parameters are given in Table 7, including the total energy of accelerated particles
 462 integrated above 1 GeV for protons, and above 511 keV for electrons. We adjusted the ratio
 463 of electrons-to-protons to differentiate between bremsstrahlung- and hadronic-dominated
 464 models. A ratio $\eta_e/\eta_p \sim 0.01$ is seen in cosmic rays at Earth around 10 GeV (Gaisser
 465 1990), but an even lower ratio ~ 0.001 may be expected from diffusive shock acceleration
 466 models (Reynolds 2008). We cannot robustly constrain η_e/η_p through our fits, so we choose
 467 characteristic values for each scenario. While the chosen parameters are not unique in their
 468 ability to fit the broadband spectrum, they are representative.

469 Under our simple assumptions, a single zone with a single particle distribution for both
 470 electrons and protons, we find that only hadronic models can reproduce both the observed
 471 radio and γ -ray spectra. For $\eta_e/\eta_p = 0.001$ we find a momentum cutoff of 10 GeV/c and
 472 a magnetic field of $\sim 90 \mu\text{G}$. Decreasing η_e/η_p results in a higher magnetic field strength
 473 to simultaneously fit the synchrotron normalization and break in the radio. Bremsstrahlung
 474 dominates over neutral pion decay when $\eta_e/\eta_p \geq 0.05$, but there is no combination of
 475 magnetic field strength and momentum cutoff that can simultaneously produce the observed
 476 SED from one electron population, as can be seen in Figure 7. To produce a model in which
 477 IC emission dominates, we must adopt a density of $\sim 0.1 \text{ cm}^{-3}$, which is well below gas
 478 density estimates. Therefore an IC-dominated model is unlikely, and furthermore, cannot
 479 produce a good fit to the data. The energetics of our hadronic model indicate $\sim 3 \times 10^{49}$ erg
 480 in accelerated cosmic ray protons and nuclei, which is comparable to that estimated for
 481 other old SNRs in a dense environment detected by *Fermi*.

482 The failure of bremsstrahlung-dominated models is largely due to an inability to fit
 483 both the observed spectral breaks in the radio and γ -rays. To explain synchrotron emission
 484 at a peak frequency ν from an electron in a magnetic field B, requires the electron have an

485 energy $E = 14.7(\nu_{\text{GHz}}/B_{\mu\text{G}})^{1/2}$ GeV (Reynolds 2008). For the observed radio break at ~ 6
 486 GHz and γ -ray break at ~ 1 GeV to be explained by the same electron population requires
 487 a magnetic field of ~ 1 mG, which is far in excess of the magnetic field expected for a SNR
 488 in such an evolved stage (unless the density is very high $\gtrsim 10^4$ cm $^{-3}$). However, molecular
 489 clouds have a well-known multiphase structure, so the density of HB 21 is unlikely to be
 490 uniform, and the one-zone approximation may be overly simplistic.

491 We therefore explored relaxing the single-zone assumption by modeling the radio and
 492 γ -ray emission as dominated by distinct regions. Allowing the normalization and spectrum
 493 of the radio emission to be separately fit from γ -rays is physically motivated. Radio emission
 494 is observed from dense filaments, but globally may be dominated by diffuse gas that fills
 495 a larger volume. For SNRs W44 and IC 443 the observed proton index from π^0 -decay
 496 emission is softer than the electron index inferred from the radio spectrum (Ackermann
 497 et al. 2013b).

498 In this two-zone scenario, we found that both bremsstrahlung- and hadronic-dominated
 499 models can fit the data. The cutoff in the accelerated particle spectrum responsible for
 500 γ -rays need not match that responsible for the radio emission, due to the different physical
 501 conditions. It is also possible that high-energy CR electrons may cool in the dense filaments
 502 formed by shock-interaction with molecular clumps, or that CR protons may have largely
 503 escaped from the SNR (Aharonian & Atoyan 1996; Malkov et al. 2011). In the latter case,
 504 we would expect that nearby clouds could be illuminated by the escaping CRs, but the
 505 geometry of the clouds in relation to HB 21 is not well known. While multi-zone models
 506 appear as feasible as single zone models, they are not well constrained due to the poor
 507 spatial resolution of the data at γ -rays and high-frequency radio. The energy in CRs in
 508 bremsstrahlung-dominated two-zone models is several times 10^{48} ergs, with a comparable
 509 energy in accelerated nuclei and leptons.

Table 6. *WMAP* Flux Density for HB 21. Five bands are analyzed with effective central frequencies (ν_{eff}) of 23 to 93 GHz (see §3).

Band	ν_{eff} (GHz)	beam FWHM ($^{\circ}$)	Flux Density (Jy)
K	22.7	0.93	34 ± 3
Ka	33.0	0.68	24 ± 4
Q	40.6	0.53	20 ± 5
V	60.5	0.35	17 ± 8
W	93.0	0.23	56^{a}

^a 2σ upper limit.

Table 7. One-Zone Model Parameters

Model	Index	p_{max} [GeV/c]	n_{H} [cm^{-3}]	B_{tot} [μG]	η_e/η_p	W_p [erg]	W_e [erg]
IC	1.76	100	0.1	2	1	1.3×10^{50}	2.1×10^{51}
Brems.	1.76	19	15	24	0.1	6.4×10^{48}	3.0×10^{48}
π^0 -decay	1.76	8.1	15	140	0.001	3.0×10^{49}	1.1×10^{47}

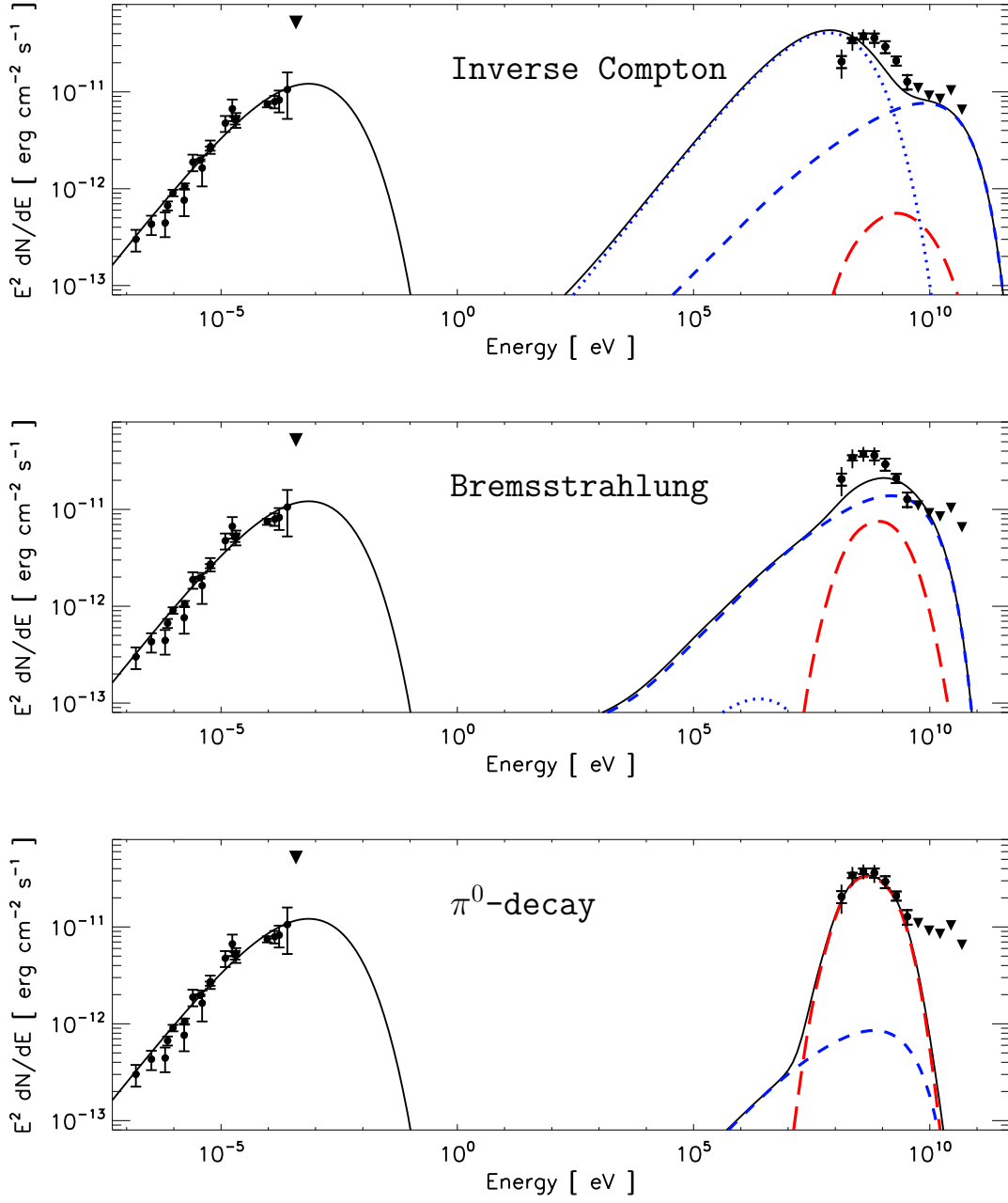


Fig. 7.— Single-zone models for which IC (top), bremsstrahlung (middle) and π^0 -decay (bottom) are the dominant emission mechanism (see Table 7 for parameters). In each model the radio data are fit with a synchrotron component, shown as a black curve. The individual contributions of π^0 -decay (long dashed), bremsstrahlung (short dashed), and IC emission from CMB (dotted) are shown. The sum of the γ -ray emission is shown by the solid curve. The leptonic and hadronic components are colored blue and red, respectively.

510 **4.2. HB 21 and the population of detected γ -ray SNRs**

511 Here we briefly discuss HB 21 in comparison to other γ -ray SNRs known to be
 512 interacting with molecular clouds. The total luminosity of HB 21 above 100 MeV at a
 513 distance of 1.7 kpc is $(3.3 \pm 0.6) \times 10^{34}$ erg s⁻¹. Other γ -ray-detected MM SNRs, such as
 514 W44 and IC 443, have luminosities of $\sim 10^{35}$ erg s⁻¹ and associated cloud masses of $> 10^4$
 515 M_{\odot} . While the total CO line emission along the line of sight to HB 21 indicates a large
 516 cloud mass, this could be due to the Cygnus OB7 complex, which lies along the line of
 517 sight at a similar velocity to HB 21, but at a distance of only 0.8 kpc, between us and the
 518 SNR. It is therefore possible that the low luminosity of HB 21 is due to the SNR currently
 519 encountering only a relatively small reservoir of material.

520 Flat radio indices, as for HB 21, are observed for other γ -ray detected SNRs known to
 521 be interacting with molecular clouds, such as IC 443 and W44. Leahy (2006) proposed two
 522 mechanisms to produce the observed flat spectrum: ionization losses due to emission from
 523 regions of high density, and low-frequency absorption by thermal electrons in the post-shock
 524 cooling regions. Alternatively, Uchiyama et al. (2010) proposed that re-acceleration
 525 takes place in the compressed cloud, resulting in a hardening of the spectrum of existing
 526 accelerated particles. Though it is likely interacting with a less-dense environment than
 527 HB 21, the latter model was shown to plausibly explain radio and γ -ray emission from SNR
 528 S147 (Katsuta et al. 2012).

529 HB 21 shows a cutoff or break in the γ -ray spectrum mirroring that of the underlying
 530 particle spectrum, which is typical of middle-aged SNRs detected by the LAT (e.g. the
 531 Cygnus Loop, Katagiri et al. 2011, and W28, Abdo et al. 2010a). This is in agreement
 532 with the circumstantial evidence for HB 21 itself to be a middle-aged/old remnant (see §1).
 533 Given the long timescales for radiative losses via proton-proton collision, bremsstrahlung
 534 or synchrotron losses for GeV particles, it is unlikely that such spectral curvature is

535 produced by radiative losses. Several mechanisms have been proposed, including runaway
 536 CRs illuminating nearby clouds (Gabici et al. 2009), the aforementioned re-acceleration
 537 in highly-compressed shocks at the interaction sites (Uchiyama et al. 2010), and magnetic
 538 damping of Alfvén waves in a partially ionized medium that leads to a break in the particle
 539 spectrum (Malkov et al. 2011). All these mechanisms appear viable for the case of HB 21,
 540 and could produce different particle distributions for electrons and protons remaining in
 541 the SNR. Given the many shared similarities with other MM SNRs, HB 21 appears to be
 542 an extension of this γ -ray class to lower luminosities.

543 5. Summary

544 We analyzed *Fermi* LAT γ -ray data from the region around HB21, a MM SNR. We
 545 detect significant γ -ray emission ($\sim 29\sigma$) associated with the remnant. The emission is best
 546 modeled by a disk centered at $(l,b) = (88^\circ 75 \pm 0^\circ 04, +4^\circ 65 \pm 0^\circ 06)$ with a radius $r = 1^\circ 19$
 547 $\pm 0^\circ 06$ with a systematic uncertainty on the position of $\sim 0^\circ 25$ and on the radius of $\sim 0^\circ 24$,
 548 so it is well-resolved by the LAT for energies greater than 1 GeV. The γ -ray emission
 549 extends over the whole area of the non-thermal radio shell, larger than the X-ray emitting
 550 thermal core. The emission in γ -rays may extend beyond the radio shell in a region rich of
 551 interstellar matter in the north western part of the SNR. Furthermore, the brightest γ -ray
 552 emitting region coincides with known shocked molecular clumps. Both results are suggestive
 553 that collisions of shock-accelerated particles with interstellar matter are responsible for the
 554 observed γ -ray emission. No spectral variations across the γ -ray emitting region that would
 555 further support this hypothesis were detected with the current observations.

556 The spectrum is best modeled by a curved function, indicative of a cutoff or break
 557 in the spectrum of the accelerated particles, typical of middle-aged/old SNRs in a dense
 558 interstellar environment. The total γ -ray luminosity of HB 21 above 100 MeV is estimated

559 to be $(3.3 \pm 0.6) \times 10^{34}$ erg s⁻¹, fainter than other SNRs interacting with molecular clouds
 560 detected by the LAT. This can be explained by the lower mass of the molecular clouds
 561 supposed to be in interaction with the remnant.

562 Reichardt et al. (2012) recently reported a lower luminosity for HB 21. We assume a
 563 distance of 1.7 kpc, based on the arguments of Byun et al. (2006), while their work assumes
 564 a nearer distance of 0.8 kpc adopted in numerous earlier works. Taking this difference into
 565 account, our values of the 0.1-10 GeV flux and luminosity of SNR HB 21 are in agreement.
 566 Even considering statistical uncertainties only, we do not find any significant evidence for
 567 spectral variations across the SNR, as suggested for cloud NW and A in their work.

568 We complement the γ -ray analysis by exploiting the *WMAP* 7-year observations from
 569 23 to 93 GHz, obtaining the first detections of HB 21 at these energies. By combining
 570 *WMAP* with lower-energies radio observations we find that the radio spectral index of
 571 HB 21 steepens significantly above 10 GHz. This spectral feature in the radio helps to
 572 constrain the relativistic electron spectrum and constrain possible physical parameters in
 573 simple non-thermal radiation models.

574 An IC origin of the γ -ray emission is disfavored because it would require unrealistically
 575 low interstellar densities in order to prevent bremsstrahlung from dominating. π^0 decay
 576 due to nuclei interactions can reproduce the data well. Bremsstrahlung and synchrotron
 577 emission from a single population of energetic electrons cannot reproduce both the γ -ray
 578 and radio SEDs. Based on the most likely values for the ISM densities over the volume
 579 of the remnant, in the hadronic-dominated scenario accelerated nuclei contribute a total
 580 energy of $\sim 3 \times 10^{49}$ ergs. This is reduced to several times 10^{48} ergs under a two-zone
 581 bremsstrahlung-dominated model, with a comparable energy in leptonic CRs.

582 The *Fermi*-LAT Collaboration acknowledges generous ongoing support from a number
 583 of agencies and institutes that have supported both the development and the operation of the

584 LAT as well as scientific data analysis. These include the National Aeronautics and Space
585 Administration and the Department of Energy in the United States, the Commissariat à
586 l’Energie Atomique and the Centre National de la Recherche Scientifique/Institut National
587 de Physique Nucléaire et de Physique des Particules in France, the Agenzia Spaziale
588 Italiana and the Istituto Nazionale di Fisica Nucleare in Italy, the Ministry of Education,
589 Culture, Sports, Science and Technology (MEXT), High Energy Accelerator Research
590 Organization (KEK) and Japan Aerospace Exploration Agency (JAXA) in Japan, and the
591 K. A. Wallenberg Foundation, the Swedish Research Council and the Swedish National
592 Space Board in Sweden. Additional support for science analysis during the operations
593 phase is gratefully acknowledged from the Istituto Nazionale di Astrofisica in Italy and the
594 Centre National d’Études Spatiales in France.

595 The Lovell Telescope is owned and operated by the University of Manchester as part
596 of the Jodrell Bank Centre for Astrophysics with support from the Science and Technology
597 Facilities Council of the United Kingdom. The Westerbork Synthesis Radio Telescope is
598 operated by Netherlands Foundation for Radio Astronomy, ASTRON.

REFERENCES

599

600 Abdo, A. A., et al. 2009a, *ApJ*, 706, L1

601 —. 2009b, *Astroparticle Physics*, 32, 193

602 —. 2010a, *ApJ*, 718, 348

603 —. 2010b, *ApJ*, 722, 1303

604 —. 2010c, *Science*, 327, 1103

605 —. 2010d, *ApJ*, 712, 459

606 —. 2011, *ApJ*, 734, 28

607 —. 2013, *ApJS*, 208, 17

608 Acciari, V. A., et al. 2011, *ApJ*, 730, L20

609 Ackermann, M., et al. 2011, *Science*, 334, 1103

610 —. 2012a, *ApJ*, 750, 3

611 —. 2012b, *Astroparticle Physics*, 35, 346

612 —. 2012c, *A&A*, 538, A71

613 —. 2013a, *Science*, 339, 807

614 —. 2013b, *Science*, 339, 807

615 Aharonian, F., et al. 2007, *A&A*, 464, 235

616 Aharonian, F. A., & Atoyan, A. M. 1996, *A&A*, 309, 917

617 Albert, J., et al. 2007, *ApJ*, 664, L87

- 618 Atwood, W. B., et al. 2009, ApJ, 697, 1071
- 619 Byun, D.-Y., Koo, B.-C., Tatematsu, K., & Sunada, K. 2006, ApJ, 637, 283
- 620 Case, G. L., & Bhattacharya, D. 1998, ApJ, 504, 761
- 621 Castro, D., & Slane, P. 2010, ApJ, 717, 372
- 622 Dame, T. M., Hartmann, D., & Thaddeus, P. 2001, ApJ, 547, 792
- 623 Dame, T. M., & Thaddeus, P. 2011, ApJ, 734, L24
- 624 de Palma, F., Brandt, T. J., Johannesson, G., Tibaldo, L., & for the Fermi LAT
625 collaboration. 2013, ArXiv e-prints
- 626 Drury, L. O. . 2012, Astroparticle Physics, 39, 52
- 627 Flower, D. R., & Pineau des Forêts, G. 1999, MNRAS, 308, 271
- 628 Gabici, S., Aharonian, F. A., & Casanova, S. 2009, MNRAS, 396, 1629
- 629 Gaisser, T. K. 1990, Cosmic rays and particle physics
- 630 Gao, X. Y., Han, J. L., Reich, W., Reich, P., Sun, X. H., & Xiao, L. 2011, A&A, 529, A159
- 631 Giordano, F., et al. 2012, ApJ, 744, L2
- 632 Giuliani, A., et al. 2011, ApJ, 742, L30
- 633 Green, D. A. 2009, Bulletin of the Astronomical Society of India, 37, 45
- 634 Grenier, I. A., Casandjian, J.-M., & Terrier, R. 2005, Science, 307, 1292
- 635 Hewitt, J. W., Grondin, M.-H., Goumar-Lemoine, M., Reposuer, T., Ballet, J., & others.
636 2012, ApJ, in print

- 637 Hewitt, J. W., Yusef-Zadeh, F., & Wardle, M. 2009, *ApJ*, 706, L270
- 638 Hill, L. E. 1974, *MNRAS*, 169, 59
- 639 Houck, J. C., & Allen, G. E. 2006, *ApJS*, 167, 26
- 640 Houck, J. C., & Denicola, L. A. 2000, in *Astronomical Society of the Pacific Conference*
641 *Series*, Vol. 216, *Astronomical Data Analysis Software and Systems IX*, ed.
642 N. Manset, C. Veillet, & D. Crabtree, 591
- 643 Janssen, G. H., Stappers, B. W., Braun, R., van Straten, W., Edwards, R. T., Rubio-Herrera,
644 E., van Leeuwen, J., & Weltevrede, P. 2009, *A&A*, 498, 223
- 645 Jarosik, N., et al. 2011, *ApJS*, 192, 14
- 646 Karlsson, N., & Kamae, T. 2008, *ApJ*, 674, 278
- 647 Katagiri, H., et al. 2011, *The Astrophysical Journal*, 741, 44
- 648 Katsuta, J., et al. 2012, *ApJ*, 752, 135
- 649 Knoedlseder, J., Oberlack, U., Diehl, R., Chen, W., & Gehrels, N. 1996, *A&AS*, 120, C339
- 650 Koo, B.-C., & Heiles, C. 1991, *ApJ*, 382, 204
- 651 Koo, B.-C., Rho, J., Reach, W. T., Jung, J., & Mangum, J. G. 2001, *The Astrophysical*
652 *Journal*, 552, 175
- 653 Kothes, R., Fedotov, K., Foster, T. J., & Uyaniker, B. 2006, *A&A*, 457, 1081
- 654 Lande, J., et al. 2012, *ApJ*, 756, 5
- 655 Lazendic, J. S., & Slane, P. O. 2006, *ApJ*, 647, 350
- 656 Leahy, D. A. 2006, *ApJ*, 647, 1125

- 657 Leahy, D. A., & Aschenbach, B. 1996, *A&A*, 315, 260
- 658 Leahy, D. A., & Roger, R. S. 1998, *ApJ*, 505, 784
- 659 Lorimer, D. R., et al. 2006, *MNRAS*, 372, 777
- 660 Malkov, M. A., Diamond, P. H., & Sagdeev, R. Z. 2011, *Nature Communications*, 2
- 661 Mattox, J. R., et al. 1996, *ApJ*, 461, 396
- 662 Mavromatakis, F., Xilouris, E. M., & Boumis, P. 2007, *Astronomy and Astrophysics*, 461,
663 991
- 664 Nolan, P. L., et al. 2012, *ApJS*, 199, 31
- 665 Protassov, R., van Dyk, D. A., Connors, A., Kashyap, V. L., & Siemiginowska, A. 2002,
666 *ApJ*, 571, 545
- 667 Reichardt, I., de Oña-Wilhelmi, E., Rico, J., & Yang, R. 2012, *A&A*, 546, A21
- 668 Reynolds, S. P. 2008, *ARA&A*, 46, 89
- 669 —. 2009, *ApJ*, 703, 662
- 670 Rho, J., & Petre, R. 1998, *ApJ*, 503, L167
- 671 Shinn, J.-H., Koo, B.-C., Burton, M. G., Lee, H.-G., & Moon, D.-S. 2009, *ApJ*, 693, 1883
- 672 Smith, D. A., et al. 2008, *A&A*, 492, 923
- 673 Sturmer, S. J., Skibo, J. G., Dermer, C. D., & Mattox, J. R. 1997, *ApJ*, 490, 619
- 674 Uchiyama, Y., Blandford, R. D., Funk, S., Tajima, H., & Tanaka, T. 2010, *ApJ*, 723, L122
- 675 Voges, W., et al. 1999, *A&A*, 349, 389

⁶⁷⁶ Wang, R.-B., & Hirovani, K. 2011, ApJ, 736, 127

⁶⁷⁷ Webb, G. M., Drury, L. O., & Biermann, P. 1984, A&A, 137, 185

⁶⁷⁸ Weiland, J. L., et al. 2011, ApJS, 192, 19

⁶⁷⁹ Yusef-Zadeh, F., Wardle, M., Rho, J., & Sakano, M. 2003, ApJ, 585, 319